

Enabling freehand lateral scanning of optical coherence tomography needle probes with a magnetic tracking system

Boon Y. Yeo,^{1*} Robert A. McLaughlin,¹ Rodney W. Kirk,¹ and David D. Sampson,^{1,2}

¹Optical + Biomedical Engineering Laboratory, School of Electrical, Electronic and Computer Engineering, University of Western Australia, Crawley WA 6009, Australia

²Centre for Microscopy, Characterisation & Analysis, University of Western Australia, Crawley WA 6009, Australia

*yeob01@student.uwa.edu.au

Abstract: We present a high-resolution three-dimensional position tracking method that allows an optical coherence tomography (OCT) needle probe to be scanned laterally by hand, providing the high degree of flexibility and freedom required in clinical usage. The method is based on a magnetic tracking system, which is augmented by cross-correlation-based resampling and a two-stage moving window average algorithm to improve upon the tracker's limited intrinsic spatial resolution, achieving 18 μm RMS position accuracy. A proof-of-principle system was developed, with successful image reconstruction demonstrated on phantoms and on *ex vivo* human breast tissue validated against histology. This freehand scanning method could contribute toward clinical implementation of OCT needle imaging.

© 2012 Optical Society of America

OCIS codes: (170.4500) Optical coherence tomography; (150.6910) Three-dimensional sensing; (330.4150) Motion detection.

References and links

1. B. E. Bouma and G. J. Tearney, "Power-efficient nonreciprocal interferometer and linear-scanning fiber-optic catheter for optical coherence tomography," *Opt. Lett.* **24**(8), 531–533 (1999).
2. P. R. Herz, Y. Chen, A. D. Aguirre, K. Schneider, P. Hsiung, J. G. Fujimoto, K. Madden, J. Schmitt, J. Goodnow, and C. Petersen, "Micromotor endoscope catheter for *in vivo*, ultrahigh-resolution optical coherence tomography," *Opt. Lett.* **29**(19), 2261–2263 (2004).
3. P. H. Tran, D. S. Mukai, M. Brenner, and Z. Chen, "*In vivo* endoscopic optical coherence tomography by use of a rotational microelectromechanical system probe," *Opt. Lett.* **29**(11), 1236–1238 (2004).
4. R. A. McLaughlin, J. P. Williamson, M. J. Phillips, J. J. Armstrong, S. Becker, D. R. Hillman, P. R. Eastwood, and D. D. Sampson, "Applying anatomical optical coherence tomography to quantitative 3D imaging of the lower airway," *Opt. Express* **16**(22), 17521–17529 (2008).
5. J. G. Fujimoto, S. A. Boppart, G. J. Tearney, B. E. Bouma, C. Pitris, and M. E. Brezinski, "High resolution *in vivo* intra-arterial imaging with optical coherence tomography," *Heart* **82**(2), 128–133 (1999).
6. B. E. Bouma, G. J. Tearney, H. Yabushita, M. Shishkov, C. R. Kauffman, D. DeJoseph Gauthier, B. D. MacNeill, S. L. Houser, H. T. Aretz, E. F. Halpern, and I. K. Jang, "Evaluation of intracoronary stenting by intravascular optical coherence tomography," *Heart* **89**(3), 317–320 (2003).
7. I. K. Jang, G. J. Tearney, B. MacNeill, M. Takano, F. Moselewski, N. Iftima, M. Shishkov, S. Houser, H. T. Aretz, E. F. Halpern, and B. E. Bouma, "*In vivo* characterization of coronary atherosclerotic plaque by use of optical coherence tomography," *Circulation* **111**(12), 1551–1555 (2005).
8. J. Yin, H. C. Yang, X. Li, J. Zhang, Q. Zhou, C. Hu, K. K. Shung, and Z. Chen, "Integrated intravascular optical coherence tomography ultrasound imaging system," *J. Biomed. Opt.* **15**(1), 010512 (2010).
9. X. D. Li, C. Chudoba, T. Ko, C. Pitris, and J. G. Fujimoto, "Imaging needle for optical coherence tomography," *Opt. Lett.* **25**(20), 1520–1522 (2000).
10. V. X. D. Yang, Y. X. Mao, N. Munce, B. Standish, W. Kucharczyk, N. E. Marcon, B. C. Wilson, and I. A. Vitkin, "Interstitial Doppler optical coherence tomography," *Opt. Lett.* **30**(14), 1791–1793 (2005).
11. Y. Wu, J. Xi, L. Huo, J. Padvorac, E. J. Shin, S. A. Giday, A. A. Lennon, M. I. F. Canto, J. H. Hwang, and X. Li, "Robust high-resolution fine OCT needle for side-viewing interstitial tissue imaging," *IEEE J. Sel. Top. Quantum Electron.* **16**(4), 863–869 (2010).
12. D. Lorensen, X. Yang, R. W. Kirk, B. C. Quirk, R. A. McLaughlin, and D. D. Sampson, "Ultrathin side-viewing needle probe for optical coherence tomography," *Opt. Lett.* **36**(19), 3894–3896 (2011).

13. B. C. Quirk, R. A. McLaughlin, A. Curatolo, R. W. Kirk, P. B. Noble, and D. D. Sampson, "In situ imaging of lung alveoli with an optical coherence tomography needle probe," *J. Biomed. Opt.* **16**(3), 036009 (2011).
14. N. V. Ifimtia, M. Mujat, T. Ustun, R. D. Ferguson, V. Danthu, and D. X. Hammer, "Spectral-domain low coherence interferometry/optical coherence tomography system for fine needle breast biopsy guidance," *Rev. Sci. Instrum.* **80**(2), 024302 (2009).
15. R. A. McLaughlin, B. C. Quirk, A. Curatolo, R. W. Kirk, L. Scolaro, D. Lorensen, P. D. Robbins, B. A. Wood, C. M. Saunders, and D. D. Sampson, "Imaging of breast cancer with optical coherence tomography needle probes: feasibility and initial results," *IEEE J. Sel. Top. Quantum Electron.* (2011), early access, <http://ieeexplore.ieee.org/xpl/articleDetails.jsp?arnumber=6007038>.
16. A. Curatolo, R. A. McLaughlin, B. C. Quirk, R. W. Kirk, A. G. Bourke, B. A. Wood, P. D. Robbins, C. M. Saunders, and D. D. Sampson, "Ultrasound-guided optical coherence tomography needle probe for the assessment of breast cancer tumor margins," *AJR Am. J. Roentgenol.* (to be published).
17. J. Ren, J. G. Wu, E. J. McDowell, and C. H. Yang, "Manual-scanning optical coherence tomography probe based on position tracking," *Opt. Lett.* **34**(21), 3400–3402 (2009).
18. A. Ahmad, S. G. Adie, E. J. Chaney, U. Sharma, and S. A. Boppart, "Cross-correlation-based image acquisition technique for manually-scanned optical coherence tomography," *Opt. Express* **17**(10), 8125–8136 (2009).
19. N. Weiss, T. G. van Leeuwen, and J. Kalkman, "Doppler-based lateral motion tracking for optical coherence tomography," *Opt. Lett.* doc. ID 164900 (posted 19 April 2012, to be published).
20. D. F. Leotta, P. R. Detmer, and R. W. Martin, "Performance of a miniature magnetic position sensor for three-dimensional ultrasound imaging," *Ultrasound Med. Biol.* **23**(4), 597–609 (1997).
21. O. Suess, S. Suess, S. Mularski, B. Kühn, T. Picht, S. Hammersen, R. Stendel, M. Brock, and T. Kombos, "Study on the clinical application of pulsed DC magnetic technology for tracking of intraoperative head motion during frameless stereotaxy," *Head Face Med.* **2**(1), 10 (2006).
22. C. A. Buckner, A. Venkatesan, J. K. Locklin, and B. J. Wood, "Real-time sonography with electromagnetic tracking navigation for biopsy of a hepatic neoplasm seen only on arterial phase computed tomography," *J. Ultrasound Med.* **30**(2), 253–256 (2011).
23. J. Kuipers, "Object tracking and orientation determination means, system and process," U. S. Patent 3,868,565 (Feb. 25, 1975).
24. F. H. Raab, E. B. Blood, T. O. Steiner, and H. R. Jones, "Magnetic position and orientation tracking system," *IEEE Trans. Aerosp. Electron. Syst.* **AES-15**(5), 709–718 (1979).
25. B. Lau, R. A. McLaughlin, A. Curatolo, R. W. Kirk, D. K. Gerstmann, and D. D. Sampson, "Imaging true 3D endoscopic anatomy by incorporating magnetic tracking with optical coherence tomography: proof-of-principle for airways," *Opt. Express* **18**(26), 27173–27180 (2010).
26. R. W. Prager, A. Gee, and L. Berman, "Stradx: real-time acquisition and visualization of freehand three-dimensional ultrasound," *Med. Image Anal.* **3**(2), 129–140 (1999).
27. H. Boonstra, J. W. Oosterhuis, A. M. Oosterhuis, and G. J. Fleuren, "Cervical tissue shrinkage by formaldehyde fixation, paraffin wax embedding, section cutting and mounting," *Virchows Arch. A Pathol. Anat. Histopathol.* **402**(2), 195–201 (1983).
28. B. Pritt, J. J. Tessitore, D. L. Weaver, and H. Blaszyk, "The effect of tissue fixation and processing on breast cancer size," *Hum. Pathol.* **36**(7), 756–760 (2005).
29. B. H. Yeap, S. Muniandy, S. K. Lee, S. Sabaratnam, and M. Singh, "Specimen shrinkage and its influence on margin assessment in breast cancer," *Asian J. Surg.* **30**(3), 183–187 (2007).
30. B. T. Sitzman and D. R. Uncles, "The effects of needle type, gauge, and tip bend on spinal needle deflection," *Anesth. Analg.* **82**(2), 297–301 (1996).
31. R. J. Webster III, J. S. Kim, N. J. Cowan, G. S. Chirikjian, and A. M. Okamura, "Nonholonomic modeling of needle steering," *Int. J. Robot. Res.* **25**(5-6), 509–525 (2006).
32. N. Abolhassani, R. V. Patel, and F. Ayazi, "Minimization of needle deflection in robot-assisted percutaneous therapy," *Int. J. Med. Robot.* **3**(2), 140–148 (2007).
33. P. M. Bloomfield, T. J. Spinks, J. Reed, L. Schnorr, A. M. Westrip, L. Livieratos, R. Fulton, and T. Jones, "The design and implementation of a motion correction scheme for neurological PET," *Phys. Med. Biol.* **48**(8), 959–978 (2003).
34. E. B. Blood, "Device for quantitatively measuring the relative position and orientation of two bodies in the presence of metals utilizing direct current magnetic fields," U. S. Patent 4,945,305 (July 31, 1990).
35. M. A. Nixon, B. C. McCallum, W. R. Fright, and N. B. Price, "The effects of metals and interfering fields on electromagnetic trackers," *Presence (Camb. Mass.)* **7**(2), 204–218 (1998).
36. W. Birkfellner, F. Watzinger, F. Wanschitz, R. Ewers, and H. Bergmann, "Calibration of tracking systems in a surgical environment," *IEEE Trans. Med. Imaging* **17**(5), 737–742 (1998).
37. V. Kindratenko, "A survey of electromagnetic position tracker calibration techniques," *Virtual Real. (Walth. Cross)* **5**(3), 169–182 (2000).
38. W. Ashe, "Magnetic position measurement system with field containment means," U. S. Patent 6,528,991 B2 (March 4, 2003).
39. D. Stoianovici, A. Patriciu, D. Petrisor, D. Mazilu, and L. Kavoussi, "A new type of motor: pneumatic step motor," *IEEE/ASME Trans. Mechatron.* **12**(1), 98–106 (2007).

1. Introduction

Optical coherence tomography (OCT) is an imaging modality that can generate real-time and *in vivo* images of biological tissue at micrometer-scale resolutions (1–20 μm). This allows OCT to bridge the gap between conventional high-resolution laboratory microscopy that requires the removal of tissue, and current medical imaging modalities such as ultrasound, X-ray computed tomography, and magnetic resonance imaging that lack microscopic resolution. As OCT has a limited imaging depth of 1–2 mm in turbid media, various forms of imaging probes have been designed to accommodate the need to image deeper into the human body, including endoscopic probes for hollow organ imaging [1–4], catheter probes for intravascular imaging [5–8], and the focus of this study, needle probes for interstitial imaging of solid tissues and organs [9–13].

OCT imaging probes require the incorporation of a lateral scanning mechanism to generate cross-sectional images (termed B-scans) by acquiring a sequence of individual depth scans (termed A-scans) from different lateral positions within the imaging target. Each A-scan represents the intensity of backscattered light as a function of depth along the incident beam. Successful B-scan reconstruction largely depends on accurate positioning of the A-scans relative to their true physical location. Until recently, OCT needle probes have been scanned using a motorized setup [11–13]. Whilst highly accurate, the complexity and size of such a setup makes the probe unwieldy and difficult to guide during insertion in a clinical environment. For example, imaging with needle-based OCT during breast cancer surgery [14–16] may require the needle probe to be inserted at large angles to the tissue normal in order to access a tumor. Scanning at such angles can be highly impractical with a motorized setup.

A more convenient approach is to maneuver the needle probe by hand and perform freehand lateral scanning. The elimination of bulky scanning motors and associated components facilitates the development of a miniaturized hand-held probe, and the high degree of freedom provided by a freehand scanning method aids in smooth control and guidance of the needle probe to the imaging target. However, hand motion inevitably contains variations in speed and orientation, which can result in geometric distortion in the reconstructed image.

There is some preliminary published research into methods to enable geometrically accurate reconstruction of OCT data from freehand scanning, mostly focusing on the artifacts caused by the variation in lateral scanning speed. Among these studies, Ren *et al.* [17] implemented an optical tracking method to monitor the position of an OCT probe during freehand scanning. In their method, four light emitting diodes (LEDs) mounted on a tetrahedral frame were attached to an OCT probe, and the detection of the emission from these LEDs with a camera provided sufficient position and orientation information to enable reconstruction of the A-scans in three dimensions (3D). One challenge with such an approach is the requirement to maintain a constant line of sight between the light sources and the detector, which may be unrealistic in some clinical scenarios.

Signal-based tracking methods have also been proposed. Ahmad *et al.* utilized a resampling technique that discards redundant or highly overlapping A-scans based on a cross-correlation similarity measure [18]. The technique was used to generate a set of A-scans with approximately uniform spacing, which was then scaled according to a calibration curve of the cross-correlation value versus physical distance between sequential A-scans. Another study by Weiss *et al.* employed a Doppler-based tracking method that estimates the lateral motion by analyzing the changes of phase between sequential A-scans [19]. These signal-based tracking methods are attractive as an external position sensor is not required, but it is not yet clear if such methods are able to provide sufficient direction and orientation information to enable reconstruction of a 3D scan trajectory.

Magnetic tracking is an alternative motion tracking method that has been used with other medical imaging modalities [20,21]. As magnetic fields are unimpeded by non-magnetic

objects, magnetic tracking does not require a clear line of sight between the magnetic field transmitter and the tracked OCT probe, making it well suited for clinical use. Nonetheless, a significant challenge in applying magnetic tracking to OCT imaging is the low position resolution of currently available magnetic trackers, which is typically on the order of hundreds of microns [22].

In this paper, we report the first published use of a magnetic tracking system with an OCT needle probe. The magnetic tracker was augmented by cross-correlation-based resampling [18] and a two-stage moving window average algorithm to enable high-resolution 3D position tracking and, thus, reconstruction of freehand OCT needle scans. The ability of the proposed method to correct artifacts caused by variations in scanning speed and orientation was assessed using phantom objects and an *ex vivo* human breast tissue specimen.

2. Methods

2.1. Magnetic tracking

A magnetic tracker comprises a transmitter and a sensor, each containing a set of coils that can be energized by an electrical current to generate a magnetic field (transmitter) or induced by a magnetic field to generate an electrical current (sensor) [23]. For transmitters based on a dipole excitation source, the generated field strength decreases with the inverse cube of the distance between the transmitter and the sensor [24]. The strength of the current induced in the sensor indicates the sensor's position relative to the transmitter. Currently available magnetic trackers are able to track with six degrees of freedom based on three orthogonally mounted coils in both the transmitter and the sensor. The transmitter coils are excited sequentially, each resulting in three individual signals measured in the sensor coils. At the end of a measurement cycle, a total of nine values are obtained, from which the position and orientation of the sensor can be determined in 3D.

In our experiments, a six-degree-of-freedom magnetic tracking system (3D Guidance medSAFE, mid-range transmitter and model 130 sensor, Ascension Technology, USA) was used to track the freehand scanning of an OCT needle probe. This tracker generates a magnetic field using pulsed direct current (DC) at the rate of 240 Hz. The maximum rate for a full measurement cycle (three transmitter axes) is 80 Hz but position coordinates are updated at 240 Hz, as a new solution is computed after the excitation of each transmitter coil. The recommended tracking range lies in a volume bounded by 20 cm to 36 cm along the x axis of the transmitter, and ± 20 cm along the y and z axes. Although the tracker's reported absolute accuracy of 1.4 mm RMS seems unsuitable for tracking micrometer-scale OCT scans, the reconstruction of freehand scans relies on the relative accuracy, *i.e.*, the accuracy of the position of the OCT needle probe relative to the position of the first A-scan. Over a 2 cm range, which is considerably larger than many OCT scans, the relative accuracy of the raw tracker measurements acquired within the recommended tracking range was measured to be 50-100 μm RMS, using a measurement protocol similar to that described in [25].

When synchronized to our OCT acquisition system, additional time latency was found between the acquisition of OCT and magnetic tracker data due to internal processing of each system. If uncorrected, this latency would cause A-scans to be assigned to incorrect tracker data points. An impulse motion method [26] was used to calibrate the latency, which was then subtracted from the time stamp of the tracker data. The latency was found to remain relatively constant between experiments at ~ 120 ms, suggesting that its effects could be eliminated by calibration.

2.2. Assembly of OCT needle probe and magnetic sensor

Figure 1(a) depicts a schematic of the OCT needle probe used in this study, which comprises a length of single-mode fiber to guide the light beam (shown in red) from the OCT scanner to the probe, a 270 μm length (0.25 pitch) of gradient-index (GRIN) fiber to produce a

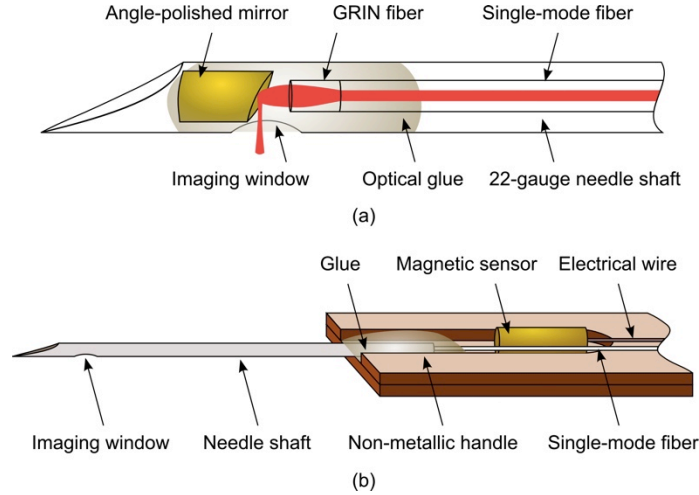


Fig. 1. Schematics of (a) the optical design of our OCT needle probe, showing the light beam (in red), and (b) the assembly of the OCT needle probe and the magnetic sensor.

collimated beam upon exiting the GRIN fiber, and an angle-polished copper mirror to reflect the beam perpendicular to the probe axis. The spot size ($1/e^2$ intensity) of the bare optical probe was measured to be $\sim 19 \mu\text{m}$. The probe was encased in a 22-gauge hypodermic needle with an outer diameter of $720 \mu\text{m}$. A small imaging window was etched in the needle shaft, approximately 8 mm from the tip, through which the A-scans were acquired. This needle probe design is based on that reported in [13], with the GRIN length adapted to produce a collimated beam at the GRIN/glue interface. The collimated beam is strongly backreflected at this interface, yielding a strong reference beam that optimizes the sensitivity for an OCT system operated in a common-path configuration [15].

The needle probe and the magnetic sensor were securely mounted on a non-metallic (wooden) handle, as shown in Fig. 1(b). The offset between the sensor and the imaging window can be described by a vector with a constant magnitude, which was measured physically, and a variable direction, which depends on the orientation of the probe. To calibrate for the offset direction, the initial orientation was measured with the needle shaft aligned parallel to the x axis of the magnetic transmitter. Because the sensor was affixed collinear with the needle shaft, the initial offset direction between them can be approximated by a $[1, 0, 0]$ vector. The initial orientation of the light beam relative to the probe axis was determined as part of the needle probe manufacturing process. By concatenating these two geometrical relationships, the motion tracked by the sensor could be transformed into the position and orientation of the imaging window, and that of the acquired A-scans. The 3D rotation matrix used in the transformation, R_{Total} , is given by

$$R_{Total} = \begin{bmatrix} \cos \psi \cos \theta & \cos \theta \sin \psi & -\sin \theta \\ \cos \psi \sin \theta \sin \varphi - \sin \psi \cos \varphi & \cos \psi \cos \varphi + \sin \psi \sin \theta \sin \varphi & \cos \theta \sin \varphi \\ \sin \psi \sin \varphi + \cos \psi \cos \varphi \sin \theta & \sin \psi \cos \varphi \sin \theta - \cos \psi \sin \varphi & \cos \theta \cos \varphi \end{bmatrix}, \quad (1)$$

which is a result of three successive rotations, such that $R_{Total} = R_x R_y R_z$, where

$$R_x = \begin{bmatrix} 1 & 0 & 0 \\ 0 & \cos \varphi & \sin \varphi \\ 0 & -\sin \varphi & \cos \varphi \end{bmatrix}, \quad R_y = \begin{bmatrix} \cos \theta & 0 & -\sin \theta \\ 0 & 1 & 0 \\ \sin \theta & 0 & \cos \theta \end{bmatrix}, \quad \text{and } R_z = \begin{bmatrix} \cos \psi & \sin \psi & 0 \\ -\sin \psi & \cos \psi & 0 \\ 0 & 0 & 1 \end{bmatrix}.$$

R_x , R_y and R_z are the rotation matrices that perform a counterclockwise rotation about the

subscripted axis and ψ , θ , and φ are, respectively, the calibrated orientation angles yaw, pitch and roll (Euler angles).

2.3. Image reconstruction using magnetic tracking and signal processing

Image reconstruction involves positioning and orienting the A-scans into the geometry from which they were acquired. The challenge in reconstructing a freehand scan is the associated variations in scanning speed and orientation. The variation in the scanning speed will cause non-uniform spatial sampling of the A-scans. Failure to account for this during image reconstruction geometrically distorts the images. Regions scanned more slowly have a higher density of A-scans and, thus, appear erroneously large, and conversely for regions through which the needle is moved more rapidly. Additionally, changes in hand orientation will rotate the light beam, and hence the acquired A-scans, both within and outside of a flat imaging plane. Failure to incorporate these orientation changes will warp the true geometry of the image due to the A-scans being incorrectly aligned parallel to each other as well as erroneously projected onto a flat reconstruction image plane. The magnetic tracker was used to detect the scan trajectory, so that both these geometric distortions could be compensated.

The position data collected by the magnetic tracker has two major limitations. Along the dominant direction of motion within a local trajectory, the position resolution is too coarse to maintain the lateral resolution of the OCT system. In the two directions orthogonal to the dominant direction, the position changes are sufficiently small that the noise in the magnetic tracking system becomes evident. To overcome these limitations, assumptions concerning the underlying motion were made to allow the use of a two-stage moving window average algorithm, which is illustrated in Fig. 2.

For clarity, we describe the algorithm here in 2D. The extension to 3D is straightforward. First, the position data (gray) is implicitly assumed to be locally linear, such that a straight line can be fitted to the subset of position data within a moving window. This window (blue) is centered at the position to be corrected, P_1 (red), as shown in Fig. 2(a). The line of best fit is calculated using principal component analysis (PCA), producing new basis vectors (v_1, v_2) (*i.e.*, principal components) that reveal the pattern of variations in the data, as shown in Fig. 2(b). In Fig. 2(c), the position data is re-expressed as a linear combination of the principal components. The first principal component, v_1 , is the least-squares best fit to the local trajectory. The second principal component, v_2 , is the least-squares best fit to the residual errors orthogonal to the first principal component. Due to our assumption of a locally linear trajectory, the variations along v_2 are regarded as noise randomly distributed about a zero mean.

To estimate sub-resolution position changes along the dominant direction, *i.e.*, along v_1 , the variation of the scanning speed is additionally assumed to be negligible within a smaller window (green) centered at P_i , as shown in Fig. 2(d). The positions in this smaller subset are projected (orange) onto v_1 to reduce noise in the data, shown in Fig. 2(e). The average of the projected positions is calculated as the corrected position (yellow). Note that the first assumption of a linear trajectory (spatially) asserts that the noise is randomly distributed about a zero mean, whereas, the second assumption of constant scanning speed asserts that the positions are changing linearly in time. The two window sizes were used to apply different weights of averaging due to these different assumptions (the smaller window for the stronger assumption of locally constant speed). The corrected position is then inversely transformed into the original coordinate frame (x, y). The original (red) and the corrected (yellow) positions are explicitly shown in Fig. 2(f) to illustrate the correction. This process is iterated over all A-scan locations, producing an enhanced spatial resolution in the final reconstruction. The extension of this algorithm to 3D includes an additional principal component v_3 , which is utilized in the same way as v_2 .

Although the local trajectory of a freehand scan is largely constant in speed, there exist regions for which this assumption is violated. For example, an abrupt stop encountered during

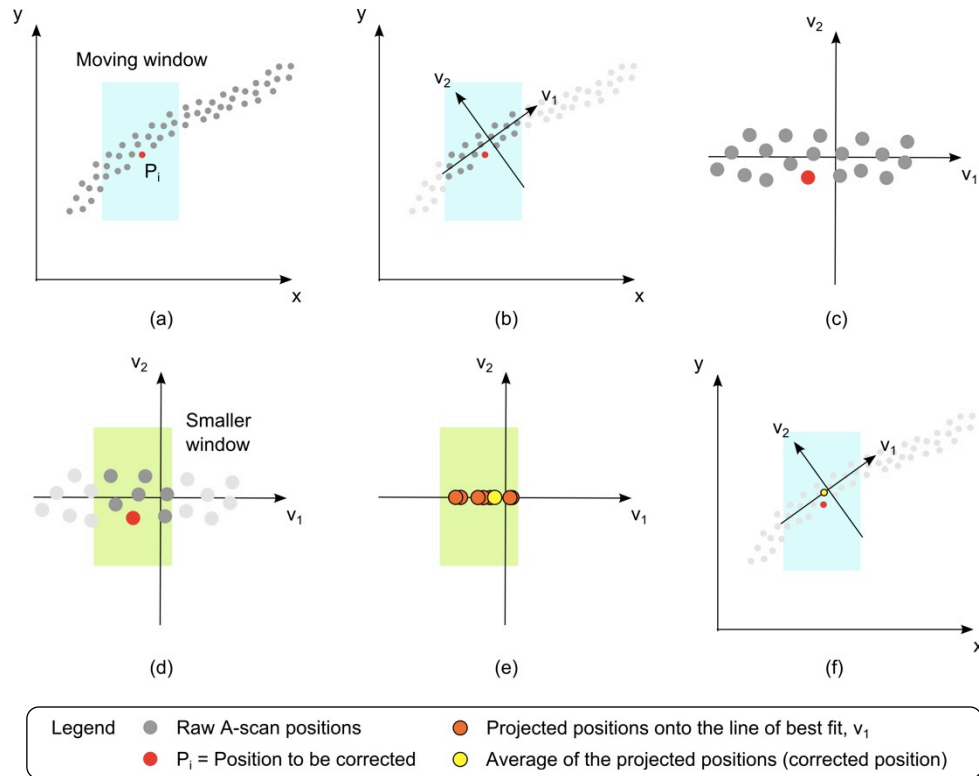


Fig. 2. Plots illustrating the two-stage moving window average algorithm in a 2D example. (a) A moving window (blue) is centered on the A-scan position to be corrected, P_1 (red). (b) PCA is performed on the subset of positions within the window, producing a least-squares best fit, denoted as v_1 , to the local trajectory. v_2 fits the residuals orthogonal to the first line of best fit. (c) The positions are re-expressed as a linear combination of the PCA basis vectors. (d) A smaller window (green) is centered on P_1 . (e) The data within this smaller window is projected (orange) onto v_1 , smoothing the noise in the minor direction of motion, v_2 . The average of the projected data is calculated as the corrected position (yellow). (f) An inverse transformation maps the corrected position onto the original coordinate frame. The corrected position is explicitly shown here relative to the original position, P_1 .

a freehand scan will result in multiple A-scans being acquired at the same position. Performing a moving average on the corresponding positions will lead to the overlapping A-scans being spaced across a small distance, distorting the size and appearance of a structure.

Therefore, prior to the refinement with the two-stage moving window average algorithm, a simplified version of the cross-correlation-based technique proposed by Ahmad *et al.* [18] was first employed to selectively discard overlapping A-scans, such that the remaining A-scans were more uniformly spaced, *i.e.*, the speed between them was made more constant. The resampling relies on the knowledge that the cross-correlation value between two A-scans decreases monotonically with increasing distance between the A-scans [18]. Briefly, an initial A-scan is selected as a reference, and the subsequently acquired A-scans are discarded until the cross-correlation with the reference A-scan decreases below an empirically chosen threshold value. This A-scan is then retained, and the process iterated by setting the newly retained A-scan as the reference. After processing the entire acquisition, the resulting set of A-scans has approximately uniform spacing. The uniform spacing achieved from this resampling step was found to greatly improve the accuracy of the reconstructed image.

Finally, each A-scan was oriented in 3D by applying the rotation matrix of Eq. (1), in which the Euler angles were given by the orientation measurements of the magnetic tracker.

The reconstruction of A-scans in six degrees of freedom produced a non-linear B-scan that followed the trajectory of the needle probe during a freehand scan.

2.4. Comparison with other image reconstruction methods

The OCT images reconstructed using the magnetic tracker method were compared against three other methods to validate the accuracy of reconstruction and to demonstrate the improvement achieved by the proposed method. First, images were reconstructed using the position data from a motorized linear translation stage (Model GTS70, Newport, USA). The translation stage has a specified accuracy of 2 μm , which allowed its position data to be used as the gold standard for validation. Second, the acquired A-scans were reconstructed using an ‘untracked’ method, which simply assumes uniform spacing between the A-scans. This naive reconstruction is representative of uncorrected freehand scanning. Third, the cross-correlation-based technique proposed by Ahmad *et al.* [18] was implemented. This technique comprises two parts: a resampling process that has been integrated into our magnetic tracker method to produce a set of uniformly spaced A-scans; and a calibration for different tissue types of the cross-correlation value versus physical distance between sequential A-scans to scale the spacing. In addition to these reconstruction methods, a histological analysis was performed in a tissue-imaging experiment to provide further validation of the biological features found in the reconstructed OCT images.

3. Imaging of tissue-mimicking phantoms

All experimental imaging in this study was performed using a spectral-domain OCT system in a common-path configuration with an optical power of 8.5 mW emitted from the imaging probe. The super-luminescent diode source (Model S-840-B-I-20, Superlum, Ireland) has a center wavelength of 840 nm with 50 nm full-width at half-maximum bandwidth, providing a theoretical axial resolution of $\sim 7 \mu\text{m}$.

The accuracy of various reconstruction methods was first assessed using a tissue-mimicking phantom object made of adhesive putty (White Tac, UHU, Germany). Four grooves with measured widths of 640 μm , 360 μm , 560 μm , and 340 μm , respectively, were imprinted on the surface of the putty to serve as features for comparison. To acquire OCT images of the phantom, the tracked needle probe was positioned adjacent to the phantom’s surface and connected to the motorized translation stage described above using a 1 m long wooden rod. This setup allows simultaneous acquisition of position data from the stage and the magnetic tracker without metal-induced magnetic field distortion. The stage was accelerated at 1 mm/s^2 to a maximum speed of 4 mm/s , then decelerated at 1 mm/s^2 covering a total scan distance of 13 mm. Acceleration and deceleration were included to simulate changes in speed present in freehand scanning. The A-scans were acquired at 5 kHz sampling rate and 15 μs exposure time.

Figure 3(a) shows the displacement profile recorded during the motorized stage scan. Three gradient triangles are shown to emphasize the changes in speed during the scan. Figure 3(b) was reconstructed based on the stage’s position data, providing the gold-standard image for the phantom. An ‘untracked’ reconstruction, assuming uniform spacing between A-scans, is presented in Fig. 3(c). It can be observed that the beginning and end portions are expanded due to the inability of this method to account for the slower scanning speeds as the stage accelerated and decelerated.

Figure 3(d) shows a tracked reconstruction using the cross-correlation-based technique described in [18]. Overall, the positioning of features by this technique shows good accuracy in this 1D motorized scanning case. However, the accuracy is significantly reduced in image areas with a poor SNR, such as at the locations of the grooves. The accuracy reduction is manifested as widening of the grooves, which is particularly evident for the larger grooves. Figure 3(e) shows a reconstruction using the magnetic tracker data with cross-correlation-based resampling and the two-stage moving window average algorithm, which maintained

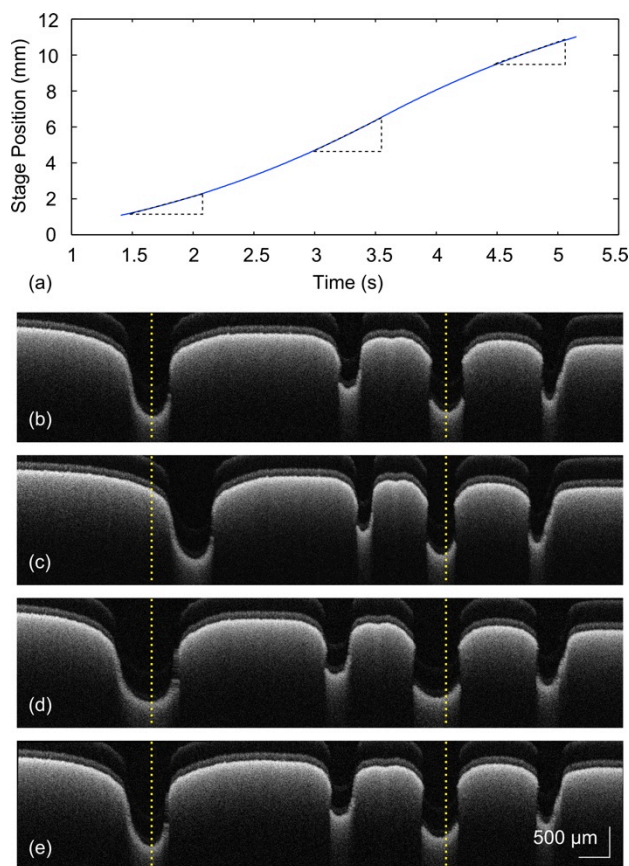


Fig. 3. (a) Displacement profile of a motorized translation stage showing acceleration during scanning. (b) Gold-standard reconstruction based on position data from the translation stage. (c) Untracked reconstruction assuming uniformly spaced A-scans. (d) Reconstruction based on the cross-correlation-based technique. (e) Reconstruction based on magnetic tracker with cross-correlation-based resampling and the two-stage moving window average algorithm. The yellow dotted lines provide a visual aid for comparing the positioning of the groove features. Scale bar = 500 μm for Parts (b)-(e).

Table 1. Accuracy of Various Reconstruction Methods

Reconstruction Method	RMS Error (μm)
Untracked	102
Cross-correlation-based technique [18]	77
Magnetic tracker	18

high accuracy even in regions having a poor SNR. A cross-correlation threshold of 0.8 was empirically chosen to reconstruct Figs. 3(d) and 3(e).

The various reconstruction methods were implemented in MATLAB[®] (R2010a, The MathWorks, Natick, Massachusetts) running on a 2.0 GHz Intel[®] Core i7-2630QM CPU with 64-bit Windows 7. The processing times for the translation stage, the cross-correlation-based, and the magnetic tracker methods were 0.63 s, 5.36 s and 7.12 s, respectively. The untracked method did not require any processing. The RMS error of each method was calculated by comparing the corresponding A-scan positions against the gold-standard translation stage position data. The results are summarized in Table 1, showing the lowest RMS error for our proposed magnetic tracker method.

In a second experiment to investigate the effect of orientation changes on the three reconstruction methods for freehand scanning, a similar phantom of the same material was

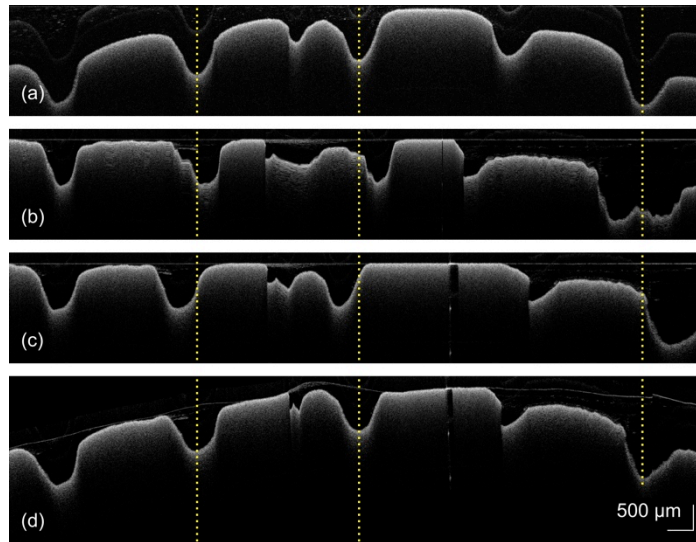


Fig. 4. Image reconstruction of a phantom with a curved surface. (a) Gold-standard image reconstructed from a motorized stage scan. Freehand scanning (with the needle probe traced along the curved surface) reconstructed using: (b) untracked; (c) cross-correlation-based; and (d) magnetic tracker methods. The magnetic tracker method reconstructed the 3D trajectory of the freehand scan ([Media 1](#)). Yellow dotted lines were drawn at the 2nd, 4th and 6th grooves for improved visual comparison. Scale bar = 500 μm for all figure parts.

made, but the grooves were formed over a curved (*i.e.*, nonplanar) surface. The gold-standard image of the phantom is shown in Fig. 4(a), which was reconstructed from a motorized stage scan at a constant speed of 2 mm/s over a range of 9 mm.

Freehand scanning was then performed by tracing the needle probe along the curved surface. The freehand scan was reconstructed as before, using the untracked, cross-correlation-based, and magnetic tracker methods. Figure 4(b) shows the untracked reconstruction, in which the artifacts caused by variations in scanning speed and orientation can be clearly observed as inaccuracies in the positions, shapes, and sizes of the grooves. As there is no information about the orientation of the beam, all A-scans were oriented vertically, reconstructing a surface that appears erroneously flat. The cross-correlation-based reconstruction in Fig. 4(c) demonstrates improved positioning accuracy, but similarly fails to account for the changes in orientation of the needle probe as it was scanned along the curved surface of the phantom. In Fig. 4(d), the magnetic tracker reconstruction exhibits a significant improvement, with the grooves and the curved surface shape showing a closer match to the gold-standard image. The same correlation threshold of 0.8 was used for both the cross-correlation-based and the magnetic tracker reconstructions.

A low-signal region that can be observed after the 4th groove in Figs. 4(b)-(d) is not an artifact but a feature corresponding to a small hole in the phantom. This feature is not seen in the gold-standard image due to a slight variation of the imaging planes between scanning with the translation stage, and the subsequent freehand scanning. Although the freehand scan occurred along a 3D trajectory with associated out-of-plane translation and rotation of the probe, the magnetic tracker reconstruction is shown here as a 2D projection image to facilitate the comparison with other methods. The non-planar B-scan reconstructed from the full 3D trajectory using the magnetic tracker method is shown in an online animation ([Media 1](#)).

4. Imaging of biological tissue

The feasibility of using the magnetic tracking method for freehand scanning of biological tissue was demonstrated on an *ex vivo* human breast tissue specimen. The study was approved by the Human Research Ethics Committee of Sir Charles Gairdner Hospital, Western

Australia, and informed consent was obtained from the patient. A 75-year-old female with a 20 mm invasive ductal carcinoma, undergoing a left mastectomy, was enrolled. The fresh (not fixed) tissue specimen was obtained during surgery, and kept hydrated in phosphate buffered saline solution until imaging (within two hours of excision).

As this experiment involved interstitial scanning of a biological tissue, the imaging planes of the gold-standard translation stage scan and the subsequent freehand scan are challenging to align. A small misalignment could result in apparent differences in the reconstructed images due to the presence of complex features in a biological tissue. Similarly, a representative histological section should be obtained as close to the OCT imaging plane as possible. To reduce issues of misalignment of the imaging planes between gold-standard translation stage scans and freehand scans, and to guide subsequent histological sectioning, an 18-gauge guide needle (38 mm length, 840 μm inner diameter) was first inserted into the tissue specimen, and was held in place for the whole duration of OCT scanning to serve as a landmark. The 22-gauge OCT needle probe was inserted into the larger guide needle shaft, which contained a 2 cm long slot to allow sufficient lateral scan range for the acquisition of A-scans. Whilst the guide needle restricts the degrees of freedom of the needle probe during a freehand scan, its use was deemed necessary to enable correlation with validation scans. The guide needle would not be required in clinical usage.

In the first scan, the OCT needle was retracted through the guide needle at a constant rate of 2 mm/s by a translation stage to generate a gold-standard image of the tissue. The probe was re-inserted into the guide needle and a freehand scan was performed by manually retracting the needle probe, with associated variations in speed and orientation. The freehand data was reconstructed using the untracked (uniform A-scan spacing), and the magnetic tracker methods. Following OCT imaging, the tissue was sampled along the length of the guide needle, parallel to the OCT imaging plane, and a hematoxylin and eosin (H&E) stained section was prepared using standard histological techniques.

Figure 5(a) shows the H&E stained histological image, with the guide needle track appearing as a localized defect (indicated by arrows). The region corresponding to the OCT translation stage scan is delineated by a dashed rectangle, and magnified in Fig. 5(b). Four features commonly found in the composition of breast tissue have been identified and labeled, including a milk duct (D), blood vessels (V), adipose tissue (A), and connective tissue (C). As shrinkage due to tissue fixation and processing is typical of histological processing [27,28], with different tissues affected to different degrees [29], the histological image is used here to provide an understanding of the biological features, rather than to validate the geometrical distance and orientation of the features found in the OCT images, which were acquired in fresh tissue.

Figure 5(c) shows the OCT gold-standard image generated from the initial motorized stage scan. Features similar to those found in the histological image can be identified, and have been labeled. Areas of adipose (A) present with a characteristic honeycomb structure, with each highly scattering cell membrane enclosing a region of low-scattering lipid. The milk duct (D) appears as a low-scattering region with a distinctive and highly scattering boundary. The endothelial walls of the blood vessel (V) are highly scattering, and the connective tissue (C) appears as a dense homogeneous area of highly scattering tissue. Such structures correlate well with previously published OCT images [15]. The subsequently performed freehand scan was first reconstructed using the untracked method, as shown in Fig. 5(d). Due to the variation in speed during the freehand scan, the A-scans have been incorrectly spaced, causing significant geometrical distortion. The field of view of this freehand scan is smaller than the stage scan due to the different extents of needle insertion into and retraction from the guide needle during the acquisition.

The same freehand data set was then reconstructed using the magnetic tracker method and the result shown in Fig. 5(e). Due to the low scattering from the adipose tissue, the cross-correlation between sequential A-scans decreases rapidly. Therefore, a slightly lower

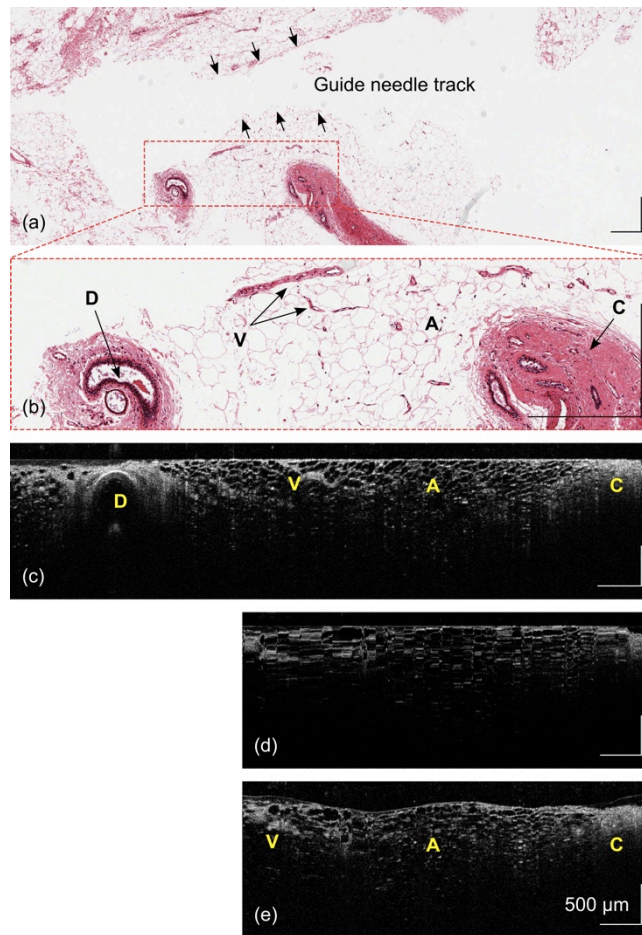


Fig. 5. (a) Histological image of a human breast tissue specimen in the vicinity of the OCT-scanned area. The guide needle track is indicated by arrows. The region scanned using the translation stage is delineated by a dashed rectangle. (b) A magnified view of the outlined region in (a), in which four features have been labeled: milk duct (D), blood vessel (V), adipose tissue (A), and connective tissue (C). (c) OCT gold-standard image reconstructed from translation stage scanning, showing features comparable to histology. (d) OCT freehand scanning reconstructed using the untracked method. Features are geometrically distorted due to variation in the scanning speed. (e) OCT freehand scanning reconstructed using the proposed magnetic tracker method. Blood vessels (V), adipose tissue (A) and connective tissue (C) are reconstructed with sizes and shapes similar to the gold-standard OCT image. Scale bars = 500 μm .

threshold value (0.75) was empirically chosen for this reconstruction to ensure sufficient spacing between A-scans. A number of biological features, such as connective tissue, adipose tissue and vasculature, can be identified. The features exhibit sizes and shapes comparable to those evident in the gold-standard image. It is noteworthy that the complex globular shape of the individual adipose cells has been maintained by the magnetic tracker method in this freehand scan. Minor differences between the gold-standard and the magnetic tracker-based images are attributed to a slight change in the imaging plane between scans. The magnetic tracker reconstruction also shows the undulation in the trajectory of the freehand scan.

5. Discussion

We have described a novel freehand scanning method for OCT needle probes using magnetic tracking. This study is the first to address the correction of artifacts caused by both the speed

variation and the changes in orientation during freehand scanning of an OCT needle probe. Additionally, we have manufactured and calibrated the first prototype of a magnetically tracked needle probe.

A number of concepts are demonstrated through the experiments presented here. First, the motorized scan with acceleration, to simulate freehand scanning, enabled assessment of the accuracy of the various reconstruction methods. The proposed magnetic tracker method achieved an accuracy of 18 μm , which was not affected by SNR, as is the case for methods that rely entirely on the image content. Second, we investigated the effect of changes in orientation on the reconstruction by performing a freehand scan, tracing the needle probe along the curved surface of a phantom. Both untracked and cross-correlation-based methods failed to account for the orientation changes, erroneously reconstructing the curved surface as flat. In addition, these methods produced 2D images, which do not reflect the true 3D freehand scan trajectory. The magnetic tracker method was shown to be able to account for both the orientation changes and the 3D scan trajectory. Finally, by testing the freehand scanning method on an *ex vivo* human breast specimen, we established that it performed adequately on biological tissue in the presence of complex features, such as the globular network of adipose tissue.

One potential confounding factor in the accuracy of reconstructions is deflection of the needle during insertion, which will alter the transformation between the magnetic sensor and the imaging window. Earlier studies have shown this deflection to decrease with larger, more rigid needles, and to be negligible for a 22-gauge needle over an insertion depth of 20 mm [30]. For bevel tip needles, a major cause of deflection is the asymmetric forces acting on the needle tip. Such deflections have been shown to be minimized by rotating the needle during insertion [31,32].

The orientation measurement in this experiment was represented with Euler angles. Such a representation is known to suffer from the ‘gimbal lock’ problem [33], which is the loss of one degree of freedom due to the overlapping of two rotational axes. This phenomenon occurs because each individual axis is evaluated independently in a fixed order when using Euler rotation matrices. For the sensor used in this experiment, yaw is measured as the rotation about the z axis of the transmitter frame, pitch is the rotation about the y' axis of the intermediate frame after the yaw rotation, and roll is the rotation about the x'' axis of the second intermediate frame after the first two rotations. When the sensor is near $\pm 90^\circ$ pitch, the rotational axes for yaw and roll overlap, resulting in a significant reduction of measurement accuracy. Nonetheless, the gimbal lock problem quickly disappears once the sensor is oriented away from the poles. In practice, this limitation could be avoided by careful orientation of the tracking system relative to the patient, so that the intended scanning trajectory does not occur along the $\pm 90^\circ$ pitch direction.

The proof-of-principle experiments in this study were performed with the setup situated away from metals. This approach, whilst being the best to mitigate metal-induced magnetic field distortion, may not be feasible in certain clinical scenarios. Further study of the sources of metal-induced distortion, including the effects of eddy currents and ferromagnetism, may be needed to ensure the system design is suitable for clinical implementation. These effects are briefly discussed below.

Eddy currents, the circulation of charge induced in nearby conductors by a changing magnetic field, lead to the generation of secondary magnetic fields that interfere with the field to be measured. The two types of magnetic trackers, alternating current (AC) and pulsed DC, interact differently with conductors. The continuously time-varying AC field induces eddy currents in each measurement cycle. Pulsed DC trackers were developed to reduce this artifact by generating pulses of DC magnetic fields, restricting the induction of eddy currents to only the rising and falling edges of the pulses [34]. By delaying the measurement until the initial eddy currents have decayed, pulsed DC tracking can avoid or reduce the distortion they cause. For example, Nixon *et al.* reported no measurable effect on pulsed DC tracking from cubes

(25 mm × 25 mm × 25 mm) of the common metals, stainless steel (316 grade), brass and aluminum, placed nearby [35].

Ferromagnetism, on the other hand, will affect both AC and pulsed DC trackers as ferromagnetic metals, such as iron, nickel, cobalt and 400 series stainless steel, retain their magnetization in the absence of an external field. There have been several attempts to correct for ferromagnetic distortion, which generally rely on interpolation or polynomial fitting techniques to estimate the true positions from a set of calibration data [36,37]. However, these calibration methods are typically time-consuming and calculation-intensive, and require recalibration as the environment changes. An alternative method that has been employed to reduce metal influence is to contain and redirect the transmitted magnetic fields such that the fields are attenuated outside of an operating volume, resulting in reduced sensitivity to metals found outside of this volume [38].

The tracking method proposed in this study has been used to reconstruct a non-planar cross-sectional B-scan from a 3D scan trajectory. The method may be extended to the acquisition of 3D OCT data volumes by incorporating an additional mechanism to rotate the needle during pullback. Such acquisitions have previously been demonstrated with fully motorized setups [12,13,15]. Use of the magnetic tracker places additional constraints upon the choice of motor, to avoid influencing the magnetic field. Non-magnetic motors designed for use with magnetic resonance imaging, such as ultrasonic motors (*e.g.*, Squiggle motors, New Scale Technologies, New York, USA) and pneumatic stepper motors [39], are potential candidates to be combined with the magnetic tracking method presented in this paper.

6. Conclusions

This paper has presented the first published use of a magnetic tracking system to reconstruct freehand scans acquired using an OCT needle probe. The proposed method substantially improves upon the intrinsic spatial resolution of the magnetic tracker by applying cross-correlation-based resampling and a two-stage moving window average algorithm. The accuracy of the improved magnetic tracking method was measured to be 18 μm RMS. The proof-of-principle system described here was validated both with phantom objects and interstitial scans of *ex vivo* human breast tissue. This freehand scanning method could contribute toward implementation of OCT needle imaging for *in vivo* clinical applications.

Acknowledgments

We gratefully thank our collaborator, Dr. Benjamin Wood, PathWest, for assisting in the processing of the breast tissue specimen and interpretation of its histology. We also thank colleagues Bryden Quirk for guidance on the construction of OCT needle probes, and Dirk Lorensen for helpful discussion on removal of fixed-pattern noise in OCT images. B. Y. Yeo is funded through grants from The Derham Green Fund, and The David & Wilma Keath Family Prescribed Private Fund, managed by Perpetual, and a SIRF scholarship from the University of Western Australia. R. A. McLaughlin is supported by funding from the Cancer Council Western Australia, and this project is supported by the National Breast Cancer Foundation, Australia.